Single-n versus multiple-n simulations of Alfvénic modes

G. Vlad[1], S. Briguglio[1], G. Fogaccia[1], V. Fusco[1], C. Di Troia[1], E. Giovannozzi[1], X. Wang[2] and F. Zonca[1,3]

[1] ENEA, Dipartimento FSN, C. R. Frascati, via E. Fermi 45, I-00044 Frascati (Roma), Italy

[2] Max-Planck-Institut für Plasmaphysik, Boltzmannstr. 2, 85748 Garching, Germany

[3] Institute for Fusion Theory and Simulation and Department of Physics, Zhejiang University, Hangzhou 310027, People's Republic of China

E-mail: `gregorio.vlad@enea.it`

Abstract. The results of a set of simulations of Alfvén modes driven by an energetic particle population are presented, with the specific aim of comparing single-n and multiple-n simulations (n being the toroidal mode number). The hybrid reduced $O(\epsilon_0^3)$ MHD gyrokinetic code HMGC is used ($\epsilon_0 \equiv a/R_0$ being the inverse aspect ratio of the torus, with a and R_0 the minor and major radius, respectively), retaining both fluid (wave-wave) and energetic particles nonlinearities. The code HMGC retains self-consistently, in the time evolution, the wave spatial structures as modified by the energetic particle (EP) term. Simulations with toroidal mode numbers $1 \leqslant n \leqslant 15$ have been considered. For the specific energetic particle drive considered, single-n simulations are either stable (n=1), or weakly unstable ($n = 2, 3, 13, 14, 15$), or strongly unstable ($4 \leqslant n \leqslant 12$), with $4 \leqslant n \leqslant 12$ modes exhibiting similar growth-rates, while $n = 4$ the largest saturated amplitude. A variety of modes are observed (TAEs, upper and lower KTAEs, EPMs). Nevertheless, no appreciable global modification of the EP density profile is observed at saturation. On the contrary, multi-n, fully nonlinear simulation exhibits an appreciable broadening of the EP radial density profile at saturation, thus showing an enhanced radial transport w.r.t. the single-n simulations. Moreover, the sub-dominant modes are strongly modified by the nonlinear coupling which results both from the MHD and from the Energetic Particle terms.

PACS numbers: 52.35.Bj, 52.35.Py, 52.55.Pi, 52.65.Ww, 52.30.Cv, 52.30.Gz, 52.55.Tn, 52.65.Rr

Submitted to: *Nuclear Fusion*

1. Introduction

The study of the effects of energetic particles (EPs), characterized by supra-thermal velocity, on magnetically confined plasmas approaching ignited conditions is a very relevant field of investigation in the magnetic confinement plasma community since some tens of years. The main concern is that the mutual interaction of globally extended Alfvén modes and EPs (as, e.g., the fusion generated alpha particles and/or the energetic ions accelerated by auxiliary heating systems) could drive shear Alfvén modes unstable and, eventually, enhance the radial transport of the EPs themselves. This can results, in turn, in increased difficulties in approaching and/or maintaining the ignited conditions (the EPs being displaced from the inner, hot core of the plasma discharge toward the edge, colder region before slowing down and heating the bulk species), or even damaging the vacuum vessel, if escaping the plasma and hitting the reaction chamber.

Experimental and theoretical research have progressed significantly on the comprehension of Alfvén modes in presence of EPs, following the recognized capital importance for the success of the next generation ignition devices like ITER [1] (see, e.g., the following review papers [2, 3, 4, 5, 6, 7, 8]). Numerical simulations, on the other hand, play an important role in the comprehension of the physics and in the explanation of the experimental results of present devices, as well as in predicting future experiments and performances of forthcoming devices (for a recent review, see, e.g., Ref. [9]). Several numerical approaches have been considered to describe the dynamics of Alfvénic modes in presence of EPs: in order of complexity, gyrofluid codes [10], extended, kinetic-MHD codes [11, 12, 13, 14, 15, 16, 17], hybrid MHD-gyrokinetic codes [18, 19, 20, 21, 22, 23, 24, 25, 26, 27] and fully gyrokinetic codes [28, 29, 30]. In this paper, we have focused on the hybrid model [18], which has shown to be a valid compromise between accuracy in description of the wave-particle interaction, and sufficiently affordable computational resource requirements. The numerical code HMGC [31, 19, 26] used in this paper will be briefly described in the next Sec. 2; for now, let us just summarize the hybrid model as a model which describes some components of the plasma using magnetohydrodynamics (MHD) equations, treating the others through the nonlinear gyrokinetic Vlasov equation (see Ref. [32] and references therein).

Whereas linear and nonlinear dynamics of single-n simulations (where n is the toroidal mode number) have been the object of wide and accurate numerical investigations (see, e.g., Ref. [8] for a exhaustive list of references), multiple-n nonlinear simulations have only recently been addressed, and in a way not yet exhaustive (see, e.g., Refs. [33, 34, 35, 36, 37, 38, 39, 40] for hybrid MHD-gyrokinetic simulations). The effect of considering simultaneously, and self-consistently, in a single numerical simulation several toroidal mode numbers evolving together is computationally challenging, but also of considerable interest because of the nonlinear coupling between modes with different toroidal mode numbers n, which can, in principle, modify qualitatively and/or quantitatively the nonlinear dynamics observed in single-n simulations. The simulations presented in this paper have been performed thanks to a grant obtained for running the

code HMGC on the new EUROfusion HPC computer Marconi-Fusion [41] (operated by CINECA, Bologna, Italy). Simulations with a dense spectrum of toroidal mode numbers $1 \leqslant n \leqslant 15$ will be presented (the limitation being imposed by computational resources available); it is worthwhile to note that evolution of $n = 0$ perturbations will not be considered in the present paper: this means that the eventual formation of so-called zonal structures by shear Alfvén waves (see, e.g., Refs. [8, 42]), which are known to be able to regulate the turbulence induced transport, will not be considered in the present simulations and will be the object of future investigations. The comparison between the set of single-n simulations and the multiple-n ones will be performed with particular emphasis on the differences regarding the energetic particle radial transport, investigating whether the so-called "domino" effect [40] is the most relevant one; to this aim we will choose a quite unstable equilibrium in order to obtain clearer evidence.

The paper is organized as follows: in Sec. 2 the numerical model considered in HMGC will be briefly presented; in Sec. 3 the details of the equilibrium and the numerical parameters considered in the simulations will be shown. Single-n (Sec. 3.1) and multiple-n (Sec. 3.2) simulations will then be described. Finally, Sec. 4 will present discussion and conclusions.

2. Numerical model

The code HMGC [31, 19, 26] is a hybrid [18] MHD-gyrokinetic code originally developed at the Frascati Laboratories. It was developed with the aim of studying the mutual effect of a population of energetic particles, as, e.g., alpha particles produced in fusion reactions, and radially extended Alfvén modes, as, e.g., Toroidal Alfvén Eigenmodes (TAEs) [43]. It describes the bulk, thermal plasma by $O(\epsilon_0^3)$ nonlinear reduced MHD equations [44], thus considering equilibria with circular shifted magnetic surfaces, assuming also zero bulk plasma pressure ($\epsilon_0 \equiv a/R_0$ is the inverse aspect ratio of the torus, a and R_0 being, respectively, the minor and major radius). The energetic particles are described by nonlinear Vlasov equation in the drift-kinetic limit, solved using the particle-in-cell technique; the two components (thermal and energetic particles) being coupled [18] via the divergence of the pressure tensor term of the EP species entering in the extended momentum equation of the bulk plasma.

The equations implemented in the code HMGC are here briefly reported for convenience; the details of their derivation can be found in Refs. [31, 19, 26, 45]. Assuming a cylindrical coordinate system (R, Z, φ) the equations which evolve the poloidal magnetic flux function ψ and the function U, related to the electrostatic potential ϕ as $U = -c\phi/B_0$, are:

$$\frac{\partial \psi}{\partial t} = \frac{R^2}{R_0} \nabla\psi \times \nabla\varphi \cdot \nabla U + \frac{B_0}{R_0} \frac{\partial U}{\partial \varphi} + \eta \frac{c^2}{4\pi} \Delta^* \psi + O(\epsilon_0^4 v_A B_\varphi) \,, \tag{1}$$

$$\hat{\rho} \left(\frac{D}{Dt} + \frac{2}{R_0} \frac{\partial U}{\partial Z} \right) \nabla_\perp^2 U + \nabla\hat{\rho} \cdot \left(\frac{D}{Dt} + \frac{1}{R_0} \frac{\partial U}{\partial Z} \right) \nabla U = \frac{1}{4\pi} \mathbf{B} \cdot \nabla \Delta^* \psi$$

$$+\frac{1}{R_0}\nabla\cdot\left[R^2(\nabla\cdot\mathbf{\Pi}_{\rm H})\times\nabla\varphi\right]+O\left(\epsilon_0^4\rho\frac{v_A^2}{a^2}\right), \tag{2}$$

where

$$\hat{\rho}=\frac{R^2}{R_0^2}\rho\,,\quad \frac{D}{Dt}=\frac{\partial}{\partial t}+\frac{R^2}{R}\nabla U\times\nabla\varphi\cdot\nabla\,,$$

$$\nabla_\perp^2\equiv\frac{1}{R}\frac{\partial}{\partial R}R\frac{\partial}{\partial R}+\frac{\partial^2}{\partial Z^2}\,,$$

with ρ the mass density, and the Grad-Shavranov operator Δ^* defined as

$$\Delta^*\equiv R\frac{\partial}{\partial R}\frac{1}{R}\frac{\partial}{\partial R}+\frac{\partial^2}{\partial Z^2}\,.$$

Moreover, the magnetic field is defined as $\mathbf{B}\equiv R_0B_0\nabla\varphi+R_0\nabla\psi\times\nabla\varphi$, B_0 is the equilibrium toroidal magnetic field at $R=R_0$, ψ is related to the parallel component of the vector potential $a_\parallel$ as $a_\parallel=(e_{\rm H}/c)(R_0/R)\psi$, v_A is the Alfvén velocity, η is the electrical resistivity and $\mathbf{\Pi}_{\rm H}$ is the energetic particle pressure tensor ("H" standing for "hot"). The code HMGC uses a coordinate system (r,θ,φ) with r the minor radius, θ and φ the poloidal and toroidal angle, respectively. Eqs. 1, 2 are discretized using finite differences in the radial coordinate, and expanding in Fourier space along the poloidal and toroidal directions.

The energetic particle pressure tensor term entering in Eq. 2 can be calculated using the gyrokinetic formalism, by directly calculating the appropriate velocity moment of the distribution function for the particle population moving in the perturbed electromagnetic field. In term of the energetic particle distribution function $\overline{F}_{\rm H}$, the explicit expression for $\mathbf{\Pi}_{\rm H}$ is:

$$\begin{aligned}\mathbf{\Pi}_{\rm H}(t,\mathbf{x})=&\frac{1}{m_{\rm H}^2}\int d\overline{Z}D_{Z_c\longrightarrow\overline{Z}}\overline{F}_{\rm H}(t,\overline{R},\overline{M},\overline{V})\\&\times\left[\frac{\Omega_{\rm H}\overline{M}}{m_{\rm H}}\mathbf{I}+\mathbf{bb}\left(\overline{V}^2-\frac{\Omega_{\rm H}\overline{M}}{m_{\rm H}}\right)\right]\delta(\mathbf{x}-\overline{\mathbf{R}})\,,\end{aligned} \tag{3}$$

with the energetic particle distribution function calculated by solving the Vlasov equation in the gyrocenter-coordinate system $\overline{Z}\equiv(\overline{R},\overline{M},\overline{V},\overline{\theta})$, where $\overline{R}$ is the gyrocenter position, $\overline{M}$ is the conserved magnetic moment, $\overline{V}$ is the parallel velocity, $\overline{\theta}$ is the gyrophase and $\mathbf{b}\equiv\mathbf{B}/B$. In Eq. 3, $\mathbf{I}$ is the unit tensor, $D_{Z_c\longrightarrow\overline{Z}}$ is the Jacobian of the transformation from canonical to gyrocenter coordinates, $\Omega_{\rm H}$ is the gyrofrequency, and $m_{\rm H},e_{\rm H}$ are the mass and the electric charge of the EPs, respectively.

The equations of motion for the energetic particles take the form:

$$\begin{aligned}\frac{d\overline{\mathbf{R}}}{dt}=&\overline{V}\mathbf{b}+\frac{e_{\rm H}}{m_{\rm H}\Omega_{\rm H}}\mathbf{b}\times\nabla\phi-\frac{\overline{V}}{m_{\rm H}\Omega_{\rm H}}\mathbf{b}\times\nabla a_\parallel+\\&\left[\frac{\overline{M}}{m_{\rm H}}+\frac{\overline{V}}{\Omega_{\rm H}}\left(\overline{V}+\frac{a_\parallel}{m_{\rm H}}\right)\right]\mathbf{b}\times\nabla\ln B\,,\end{aligned} \tag{4}$$

$$\frac{d\overline{M}}{dt}=0\,, \tag{5}$$

$$\frac{d\overline{V}}{dt} = \frac{1}{m_{\rm H}}\mathbf{b}\cdot\left\{\left[\frac{e_{\rm H}}{\Omega_{\rm H}}\left(\overline{V}+\frac{a_\parallel}{m_{\rm H}}\right)\nabla\phi+\frac{\overline{M}}{m_{\rm H}}\nabla a_\parallel\right]\times\nabla\ln B+ \frac{e_{\rm H}}{m_{\rm H}\Omega_{\rm H}}\nabla a_\parallel\times\nabla\phi\right\}-\frac{\Omega_{\rm H}\overline{M}}{m_{\rm H}}\mathbf{b}\cdot\nabla\ln B\,, \tag{6}$$

with the Vlasov equation for the gyrocenter distribution function $\overline{F}_{\rm H}$ being:

$$\left(\frac{\partial}{\partial t}+\frac{d\overline{Z}^i}{dt}\frac{\partial}{\partial\overline{Z}^i}\right)\overline{F}_{\rm H}=0\,, \tag{7}$$

where the Einstein convention on the summation over the repeated index "i" has been assumed. Note that in Eq. 6 the parallel electric field term has been neglected.

3. Numerical simulations

We will consider in the following a model equilibrium, rather than a specific experimental device, with the aim of studying how the dynamics of the EP driven Alfvénic modes changes when considering single-n or multiple-n simulations, while keeping all the other parameters fixed. A circular, shifted magnetic surface, static equilibrium has been considered, characterized by a large aspect ratio ($\epsilon_0 = 0.1$) and a parabolic safety factor profile $q(r) = q_0 + (q_a - q_0)(r/a)^2$ with $q_0 = 1.1$ and $q_a = 1.9$ being, respectively, the on-axis and edge safety factor, respectively. A bulk ion density profile $n_{\rm i}(r) \propto (q_0/q(r))^2$ has also been assumed, in order to have the toroidal gap radially aligned, for all the mode considered. Regarding the EPs, an isotropic Maxwellian distribution function has been

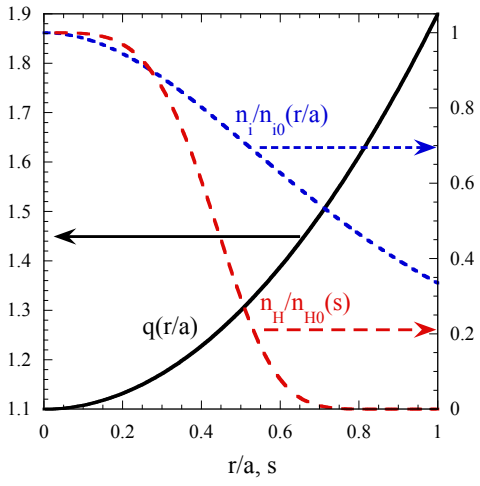

Figure 1. Safety factor q profile (solid, black curve), normalized bulk ion density $n_{\rm i}/n_{\rm i0}$ (short dashed, blue curve), and normalized EP density $n_{\rm H}/n_{\rm H0}$ (long dashed, red curve).

considered, being characterized by the ratio of EP to bulk ion mass $m_{\rm H}/m_{\rm i} = 2$, with a

radially constant EP temperature profile $T_{\rm H}/T_{\rm H0}=1$, the ratio of the on-axis EP Larmor radius to the minor radius $\rho_{\rm H0}/a=0.01$, the ratio of the on-axis EP thermal velocity to the Alfvén velocity $v_{\rm H0}/v_{\rm A0}=1$, the ratio of the on-axis EP density to the on-axis bulk ion density $n_{\rm H0}/n_{\rm i0}=1.75\times10^{-3}$ and a radial profile as $n_{\rm H}(s)=n_{\rm H0}\exp(-19.53s^4)$, s being a radial-like coordinate defined as $s\equiv\sqrt{|\psi_{\rm eq}-\psi_0|/|\psi_{\rm edge}-\psi_0|}$, with $\psi_{\rm eq}$ the equilibrium magnetic poloidal flux function and ψ_0 and $\psi_{\rm edge}$ its value at the magnetic axis and at the edge, respectively (see Fig. 1).

With the aim of comparing the single-n, Sec. 3.1, with the multiple-n, Sec. 3.2, simulations, we will use, for all these simulations, the same numerical parameters; in particular, we will consider equal grid sizes, chosen in such a way to numerically resolve the different spatial structures of the Alfvénic modes. To this aim, we can estimate the typical radial width of an MHD mode as [46] $\Delta r\propto 1/(nq')$, with "prime" indicating radial derivative, whereas $\Delta\theta\propto 1/m_{\rm max}=1/(nq_{\rm max})$ and $\Delta\varphi\propto 1/n$; thus, all the spatial characteristic lengths scale as the inverse of the toroidal mode number (here, $m_{\rm max}$ is the highest poloidal mode number retained in the simulation, and $q_{\rm max}$ the highest value of the safety factor throughout the whole radial domain). We will use, as a set of appropriate spatial mesh points for resolving perturbations characterized by toroidal mode numbers up to n=15, the following: radial mesh points for the MHD module $N_{\rm r,MHD}=300$, and radial mesh points for the gyrokinetic (GK) module, $N_{\rm r,GK}=256$, poloidal ($N_{\theta,\rm GK}=160$) and toroidal ($N_{\varphi,\rm GK}=80$) mesh points in the GK module, with the number of particles per cell $N_{\rm ppc}=8$: with these parameters, the number of spatial cells used by the gyrokinetic module is $N_{\rm cells}=N_{\rm r,GK}\times N_{\theta,\rm GK}\times N_{\varphi,\rm GK}\approx 3.3\times10^6$, and the number of simulation particles $N_{\rm p}=N_{\rm cells}\times N_{\rm ppc}\approx 26.2\times10^6$. Note that the radial meshes of the MHD and GK particle-in-cell modules can be different in HMGC.

The Fourier modes actually evolved in the different simulations are reported in Fig. 2, where also the curves $n=m/q$ corresponding to the minimum and maximum values of the safety factor $q(r)$ of the equilibrium considered ($q_{\rm min}=q_0=1.1$ and $q_{\rm max}=q_a=1.9$), are shown: note that, for each n, all the resonances given by the rational surfaces associated to the safety factor profile $q(r)$ within the plasma are included. Note also that the Fourier components in the symmetric half plane $(m,n)\longrightarrow(-m,-n)$ are included in the MHD module by considering the reality condition for $\psi(r,\theta,\varphi;t)$ and $\phi(r,\theta,\varphi;t)$ ($\psi_{-m,-n}(r;t)=\psi^*_{m,n}(r;t)$ and $\phi_{-m,-n}(r;t)=\phi^*_{m,n}(r;t)$, where $\psi_{m,n}(r;t)$ and $\phi_{m,n}(r;t)$ are, respectively, the Fourier transform of the poloidal magnetic flux function $\psi(r,\theta,\varphi;t)$ and of the electrostatic potential $\phi(r,\theta,\varphi;t)$, and the "*" indicates complex conjugate).

The initial conditions ($t=0$) for the Fourier components of the electrostatic potential have been given as:

$$\phi_{m,n}\left(\frac{r}{a}\right)=A_n 2^{2|m|}\left(\frac{r}{a}\right)^{|m|}\left(1-\frac{r}{a}\right)^{|m|}\,, \tag{8}$$

such that all the Fourier components, for fixed n, are normalized to the (complex) constant A_n, and satisfy the proper regularity condition in the limit of $r\longrightarrow 0$; initial conditions for the magnetic flux function $\psi_{m,n}$ are obtained by assigning the condition

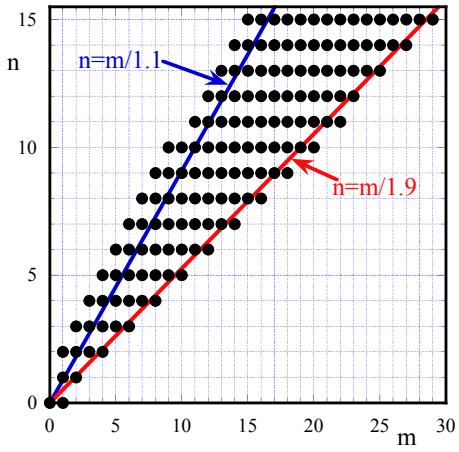

Figure 2. Fourier modes used in the simulations: equilibrium Fourier components are $(m, n) = (0, 0)$ and $(1, 0)$; the perturbed Fourier components ($n \geqslant 1$) include, for each n, the resonances given by the rational surfaces associated to the safety factor profile $q(r)$, which, for the considered equilibrium, is $1.1 \leqslant q(r) \leqslant 1.9$.

of vanishing parallel electric field in absence of electrical resistivity. In order to ensure numerical stability, HMGC requires a certain amount of diffusivity to be added in the MHD equations [31]; in particular, electric resistivity is generally sufficient for single-n simulations, whereas for multiple-n simulations also a viscosity-like term is added to the vorticity equation (Eq. 2), in the form of a term $\propto \nu\nabla_\perp^2(\nabla_\perp^2\phi)$, with ν the viscosity coefficient. For all the simulations presented hereafter, the normalized electrical resistivity and viscosity have been assigned the values of $S^{-1} = 10^{-5}$ and $\nu\tau_{A0}/a^2 = 10^{-7}$, respectively ($S$ being the Lundquist number defined as $S \equiv 4\pi a^2/(\eta c^2\tau_{A0})$, $\tau_{A0} = R_0/v_{A0}$ being the on-axis Alfvén time and $\omega_{A0} \equiv 1/\tau_{A0}$ the on-axis Alfvén frequency).

3.1. Single-n simulations

In this section we will present the results of single-n simulations, with the purpose, on one side, to characterize the considered toroidal equilibrium in presence of an EP population w.r.t. stable and unstable modes, and on the other side, to evaluate the EPs radial transport as the result of single-n nonlinear saturation. All the following single-n simulations shown hereafter have been initialized with the same value of $A_n = \bar{A}$, such to start all the simulations in the linear growth regime. In Fig. 3 the time evolution of the total (kinetic plus magnetic) MHD energy content, for each simulation with toroidal mode number n considered, is shown. Note that these single-n simulations have been performed considering constant (in time) $n = 0$ MHD fields, thus resulting in evolving the Faraday's (Eq. 1) and the MHD part of the vorticity (Eq. 2) equations in the linear

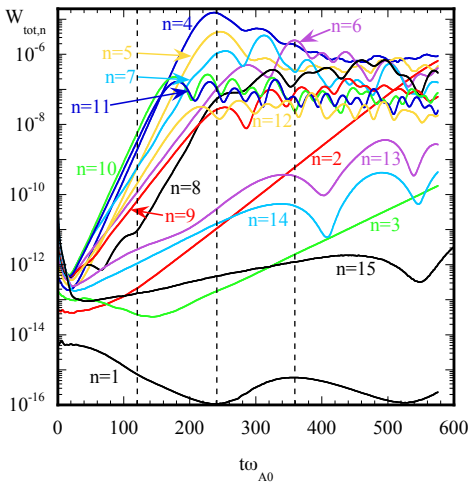

Figure 3. Single-n simulations: time evolution of the total (kinetic plus magnetic) MHD energy content for each toroidal mode number n considered $W_{\mathrm{tot},n}$. The vertical dashed lines correspond to the times of simulation $t\omega_{A0} = 120$, $t\omega_{A0} = 240$ and $t\omega_{A0} = 360$.

limit; on the other side, EPs evolution is kept fully nonlinear, which, as will be shown later on, allows the axisymmetric component of the EP density profile to evolve in time. In the simulations performed using HMGC, which is an initial value code, unstable modes grow from the "seed" of the initial conditions, and, indeed, several modes can be observed simultaneously, in particular during the initial phase of a simulation, before the strongly growing (or less damped) one fully develops and overtakes the others. The simulation with the toroidal mode number $n = 1$ results to be stable, the ones with $n = 2, 3, 13, 14, 15$ moderately unstable, whereas for $4 \leqslant n \leqslant 12$ they are observed to be strongly unstable (see Fig. 3). In Fig. 4 the growth rates of the modes observed in the single-n simulations are shown, at the reference time of $t\omega_{A0} = 120$, after Fourier analyzing the MHD fields. For some toroidal mode numbers ($n = 1, 3, 7, 8, 13$) more than a single point is, indeed, reported, each of them corresponding to a different eigenmode. The growth-rate, at first, increases with the toroidal mode number n (indeed, the EP drive is proportional to $\omega_{*\mathrm{H}} \propto k_\theta \propto n$, $\omega_{*\mathrm{H}}$ being the diamagnetic frequency of the EPs and k_θ the poloidal component of the wave vector), although heavily influenced, as n varies, by the need for minimizing the continuum damping (see later in this Section); as n increases further, the linear scaling of the drive with n is lost because of finite orbit width averaging, which yields a maximum-drive n, roughly given by $k_\perp \rho_{\mathrm{H}} \sim 1$ [47, 48, 49, 50], with $k_\perp \simeq nq(r)/r$ and ρ_{H} being the typical resonant-particle orbit width, and the subsequent growth-rate decreases.

Some more insight on the oscillation spectrum can be gained by plotting the power spectra of the electrostatic potential $|\phi(r, \omega)|^2$, as reported in Fig. 5. For example, it

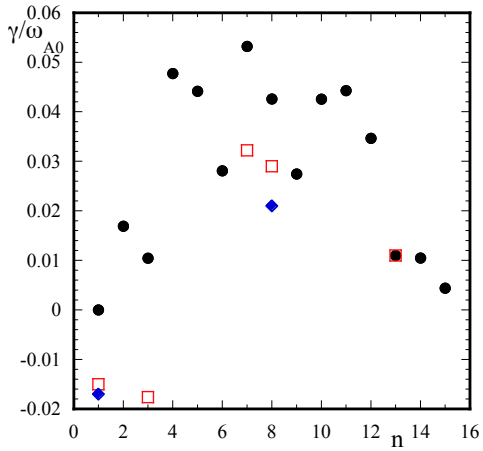

Figure 4. Single-n simulations: growth-rates of the modes as observed at $t\omega_{A0} = 120$ (for the simulations with $n = 1, 3, 7, 8, 13$ several modes are recognized, and they are reported with different symbols and colors, i.e., black, full circles, red, open squares and blue, full diamonds, respectively, in order of decreasing growth-rates).

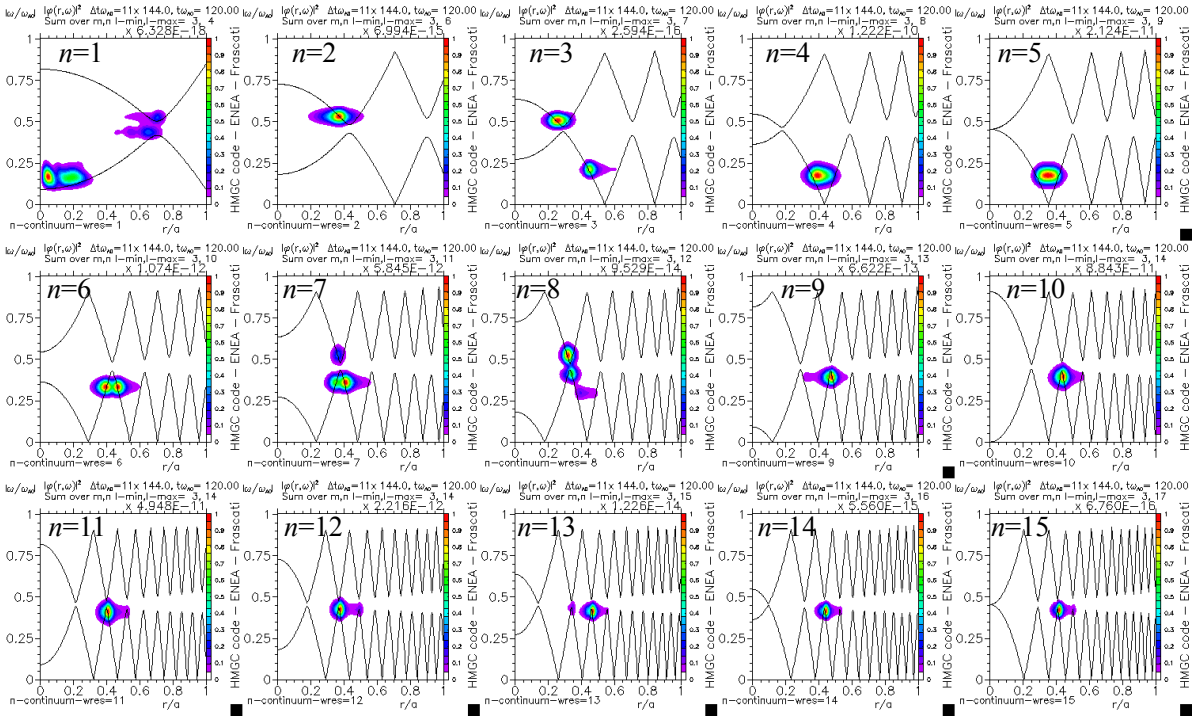

Figure 5. Single-n power spectra of the electrostatic potential $\phi(r, \omega)$ during the linear growth phase, at $t\omega_{A0} = 120$ (see the first dashed vertical line in Fig. 3), for the toroidal mode numbers $n = 1, ..., 15$; solid lines refer to the (analytically computed) Alfvén continua.

possible to recognize, for the $n = 1$ case (upper row, first frame from the left), three modes which, for the value of energetic particle density considered, results to be stable: a Global Alfvén Eigenmode (GAE [51]) localized toward the center of the plasma column, just above the lower Alfvén continuum (Alfvén continua are shown in the figures as black, solid lines) being just weakly damped, a stable Kinetic Toroidal Alfvén Eigenmode (KTAE [52]), just above the toroidal gap, and a stable Toroidal Alfvén Eigenmode (TAE [43]) within the toroidal gap, these last two modes being located radially at the position of the toroidal gap, $r/a \approx 0.7$. For the stable $n = 3$ mode, and for the $n = 4, 5$ (unstable) ones the power spectra (Fig. 5) show that the frequencies are well inside the lower Alfvén continua (EPMs [53]).

Unstable EP driven Alfvén modes will result, for a given electromagnetic field structure, from the optimal balance between, on one side, the drive given by the resonant EPs, which occurs at certain characteristic resonant frequencies (as, e.g., transit or toroidal precessional frequencies) and with the strength modulated along the radial position according to the local drive $\alpha_H = -R_0 q^2 \beta_H'$ (here β_H is the ratio of the EP thermodynamic pressure to magnetic pressure, and "prime" indicates radial derivative) and, on the other side, the dampings, which, in our model, are given primarily by the Alfvén continuum damping (apart from the small resistive and viscosity dampings retained for numerical stability purposes). The self-consistent, mutual interaction between the MHD fields and the EPs contribution will determine the self-consistent evolution of the coupled system through the linear and nonlinear, saturated phases.

In Fig. 6 the power spectra for a later time ($t\omega_{A0} = 360$), well after the saturation of all the modes with $4 \leqslant n \leqslant 12$, are shown. The power spectra for those modes are considerably modified, w.r.t. the ones shown in Fig. 5: several other peaks appear for each toroidal mode number n, mainly distributed along the corresponding Alfvén continua; these are subdominant, almost stable modes which result as a left over of the occurred saturation.

It is interesting to note how the power spectra evolve in time (time-frequency spectrograms), as the simulations pass through the linear phase toward the peak of the saturation and the following slow decay. This is shown in Fig. 7, where the power spectra shown before (see Figs. 5 and 6) are integrated in radius and plotted against time. Except for the ones referring to $n \leqslant 3$ and $n \geqslant 13$, none of which experiences saturation, all of them exhibit upward and downward chirping of the frequency. This behaviour suggests that saturation occurs because of a "net" outward radial displacement of the resonant EP fraction, as discussed, e.g., in Refs. [8, 54, 55]. Here, it is worthwhile noting that the qualitative behavior of frequency chirping in Fig. 7 is similar to that discussed in the original works by Berk, Breizman and coworkers for the beam-plasma system in the presence of sources and sinks [56, 57, 58]. However, two main differences arise in the present case, which, as discussed in Ref. [8], limit the applicability of the beam-plasma paradigm: (i) the interplay of energetic particle transport, plasma non-uniformity and finite radial mode structures; (ii) the frequency sweeping rate, which is typically non-adiabatic when energetic particle response is non-perturbative.

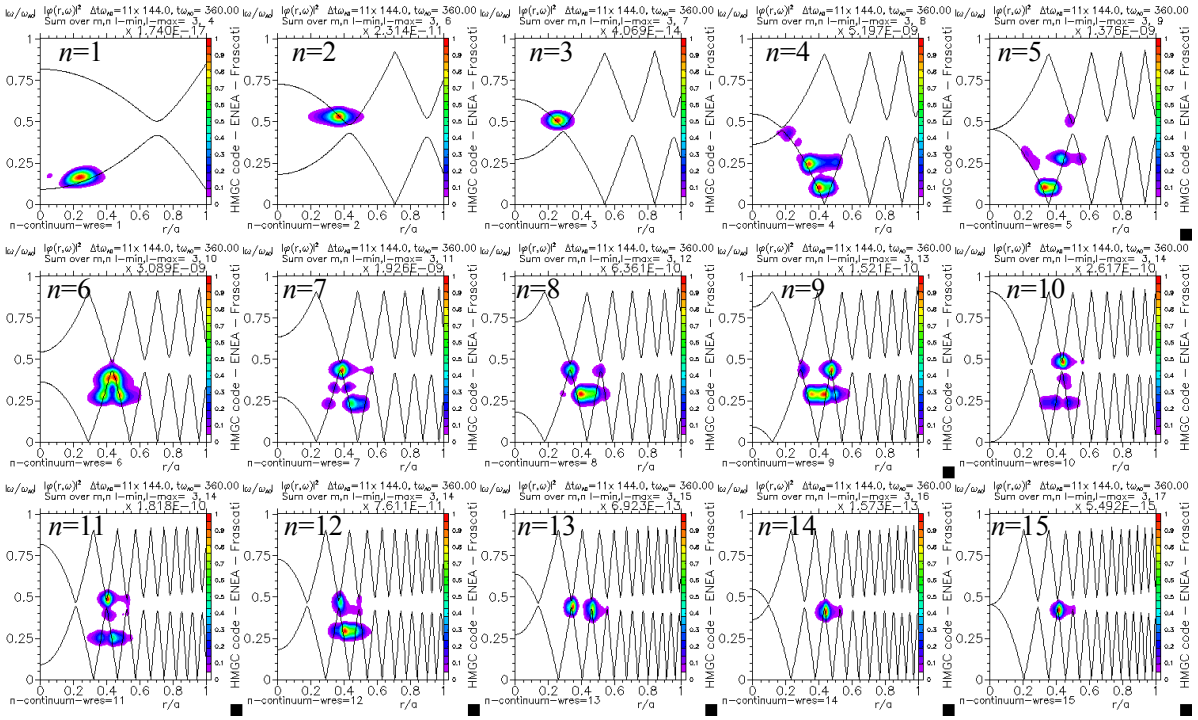

Figure 6. Single-n power spectra of the electrostatic potential $\phi(r,\omega)$, during the saturation phase of the simulation for $4 \leqslant n \leqslant 12$ modes, at $t\omega_{A0} = 360$ (see the third dashed vertical line in Fig. 3), for the toroidal mode numbers $n = 1, ..., 15$; solid lines refer to the (analytically computed) Alfvén continua.

A further characterization of the single-n simulations presented in this Section is given by the power exchange between the EPs and the wave: from its analysis it is possible to gain some hints on which fraction of the EP distribution function is mainly responsible for driving the linearly unstable modes. In Fig. 8 the power exchange in the (μ, u) plane is reported, after integrating in the whole space domain (here, μ is the (normalized to $T_{\mathrm{H}}/\Omega_{\mathrm{H0}}$) magnetic moment and u the (normalized to $\sqrt{T_{\mathrm{H}}/m_{\mathrm{H}}}$) parallel velocity the EPs will have when crossing the equatorial plane at the outermost radial position of their orbit). Also, the curve corresponding to the trapped/untrapped boundary for $r = a$ is reported (dashed curves). Different resonances are recognized to be responsible of the unstable modes: co- and/or counter-passing transit resonances (the ones outside, above and/or below, the trapped/untrapped boundary), or the toroidal precessional resonance (the ones inside the trapped/untrapped boundary). A detailed analysis of the driving resonances, which is, nevertheless, outside the scope of the present paper, can be obtained, e.g., using the Hamiltonian mapping techniques in order to generate kinetic Poincaré plots (see, e.g., Refs. [59, 60, 55]). Note that the frame corresponding to the $n = 1$ (stable) simulation is dominated by regions in the (μ, u) plane which exhibit a negative transfer of energy from the particles to the waves, i.e., a net damping contribution (blue pattern colors).

When, for unstable modes, the electromagnetic fields reach sufficiently high values,

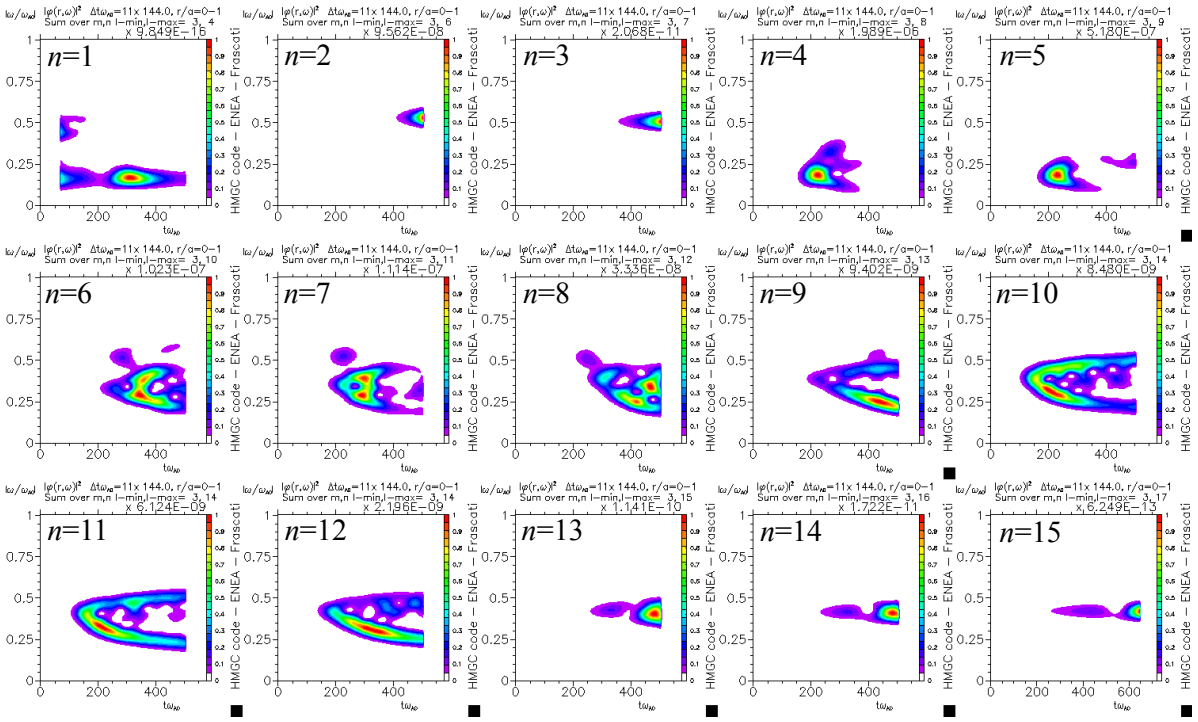

Figure 7. Single-n simulations: time-frequency spectrograms of the electrostatic potential for single-n simulations.

EPs will be scattered away from the unperturbed orbits they experience during the linear growth phase, typically resulting in the broadening of the density radial profile and, because of reducing the EP density gradient, accounting for mode saturation. Two main mechanisms have been identified as being responsible for nonlinear saturation of EP driven Alfvénic modes: the trapping of the resonant EPs in the potential well of the wave, typically occurring for modes close to marginal stability (e.g., TAEs) [61, 62, 63], and a second one characterized by macroscopic outward displacement of the EPs, experiencing a convective secular process [21, 8], occurring for strongly driven modes (e.g., EPMs [53]). As stated before, the Hamiltonian mapping techniques are suited tools to identify the mechanism underlying, generally speaking, the nonlinear dynamics of EP driven modes, and detailed analyses have been indeed already performed [60, 55]. For the single-n simulations considered in this Section, the global broadening of the (axisymmetric) radial density profile of the EPs is quite modest, almost indistinguishable for all the modes which fully enter the saturation phase ($4 \leqslant n \leqslant 12$), apart for the case of $n = 4$, shown in Fig. 9. The broadening of the radial profile is quite modest when observed on the whole (i.e., integrated on the full velocity space) EP population, while it can be shown to be much more evident when considering selectively the fraction of EPs which are resonating with the mode (see, e.g., Ref. [60, 64]). For the case of $n = 4$ simulation, the broadening of the profile, and, thus, the resulting reduction of the density gradient, occurs around $r/a \approx 0.4$: this is the radial position where the eigenfunction of the $n = 4$ linear growing mode were localized (see Fig. 5), and where

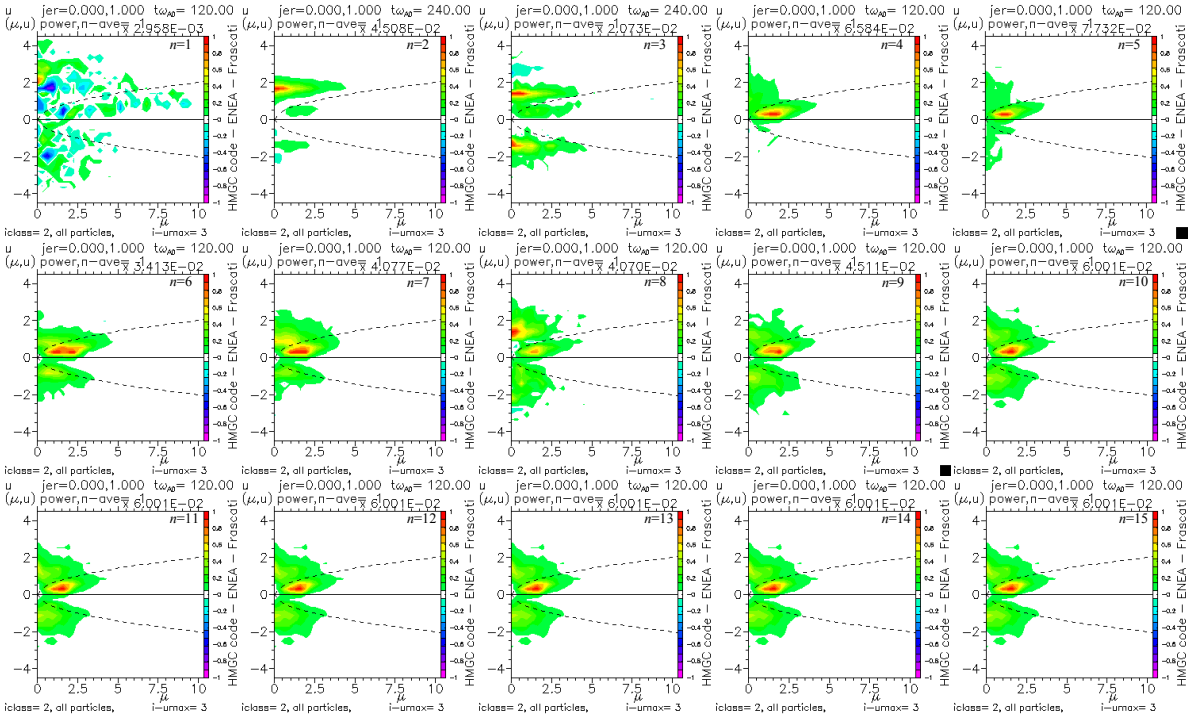

Figure 8. Single-n simulations: wave-particle power exchange in the plane (μ, u) (positive values, from white to red color pattern, correspond to particles driving the wave); $t\omega_{A0} = 120$ for all n but $n = 2, 3$ for which $t\omega_{A0} = 240$. Here $\mu = \overline{M}/(T_{\rm H}/\Omega_{\rm H0})$ is the normalized EP magnetic moment; $u = \overline{V}/\sqrt{T_{\rm H}/m_{\rm H}}$ is the normalized parallel velocity the EP will have when crossing the equatorial plane at the outermost radial position of its orbit. The curve corresponding to the trapped/untrapped boundary for $r = a$ is also reported (dashed curves).

we can expect the resonance to occur and the EP nonlinearities to be more effective.

3.2. Multiple-n simulations

In this Section, multiple-n simulations will be presented, to be compared with the set of single-n simulations presented in the previous Section, Sec. 3.1. To this purpose, we have considered the same Fourier mode spectra shown in Fig. 2, thus evolving simultaneously all the $n = 1, ..., 15$ toroidal Fourier components. The $n = 0$ Fourier components have still be considered to be fixed in time, as in the previously presented single-n simulations (see Sec. 3.1); all the numerical parameters of the simulations have been kept constant, e.g., equilibrium, spatial grids and EPs parameters.

The conventional view of the dynamics of multiple-n simulations is that, in the presence of more than one unstable mode, the strongest growing one saturates first, because of the flattening of the EP radial density profile, at least for the fraction of the EPs resonating with the mode; weaker, or even stable modes, in turn, can be driven unstable (or more unstable) because of these modifications to the EP distribution induced by the saturation of the dominant mode (see, e.g., Ref. [40]), giving rise to a sort of "domino" effects.

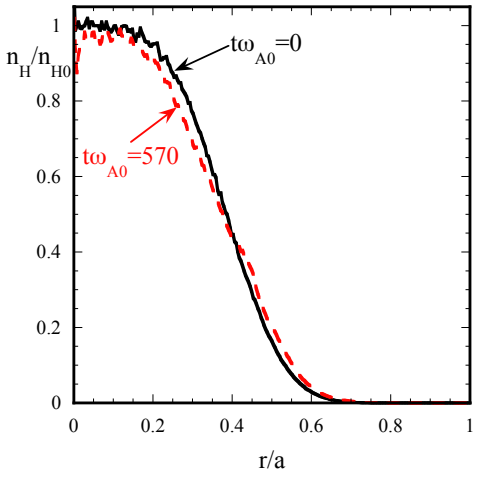

Figure 9. Single-n, $n = 4$ simulation: axisymmetric radial profile of EPs at the beginning ($t\omega_{A0} = 0$, solid, black curve) and at the end ($t\omega_{A0} = 570$, dashed, red curve) of the simulation.

The novel observations from the present simulations, as will be shown shortly in the present Section, on the contrary, suggest the following scenario: the nonlinear mode-mode coupling coming from the MHD terms and/or mediated by the EP coupling term, strongly drives sub-dominant modes already during the linear growth phase of the dominant modes; the sub-dominant modes driven nonlinearly have the radial profiles of the MHD fields ($\psi_{m,n}(r)$, $\phi_{m,n}(r)$) and their real frequencies substantially different from the ones they would have if evolved as single-n modes; all the toroidal modes saturate almost simultaneously (similar observations have been reported by Ref. [36, 65]), after inducing an enhanced (w.r.t. the single-n simulations) EP radial transport.

In Fig. 10 the total (kinetic plus magnetic) MHD energy content for each toroidal mode number n considered, $W_{\mathrm{tot},n}$, is compared with the results of the single-n simulations (already shown in Sec. 3.1, Fig. 3). Nonlinear coupling between different toroidal mode numbers are clearly observable (see, e.g., the $n \leqslant 3$ and $n \geqslant 13$ modes, for $t\omega_{A0} \gtrsim 100$). The corresponding growth of toroidal Fourier components classified as stable or weakly unstable in the single-n simulations ($n \leqslant 3$ and $n \geqslant 13$) is clearly observable. From the linear scale plot of Fig. 10 it is also noted that the single-n, $n = 4$ simulation reaches a higher overshooting value that the multiple-n one (around $t\omega_{A0} \approx 230$); nevertheless, as it will be shown later on, the radial EP transport is markedly higher in the multiple-n simulation than in the single-n ones. Note that the time duration of the multiple-n simulation shown in Fig. 10 is limited by the available elapsed time of the current Marconi-fusion queue system; similar multiple-n simulations, with a toroidal Fourier spectrum truncated earlier ($1 \leqslant n \leqslant 10$) and run for longer simulation time (same time as the single-n simulations) exhibit qualitatively the same

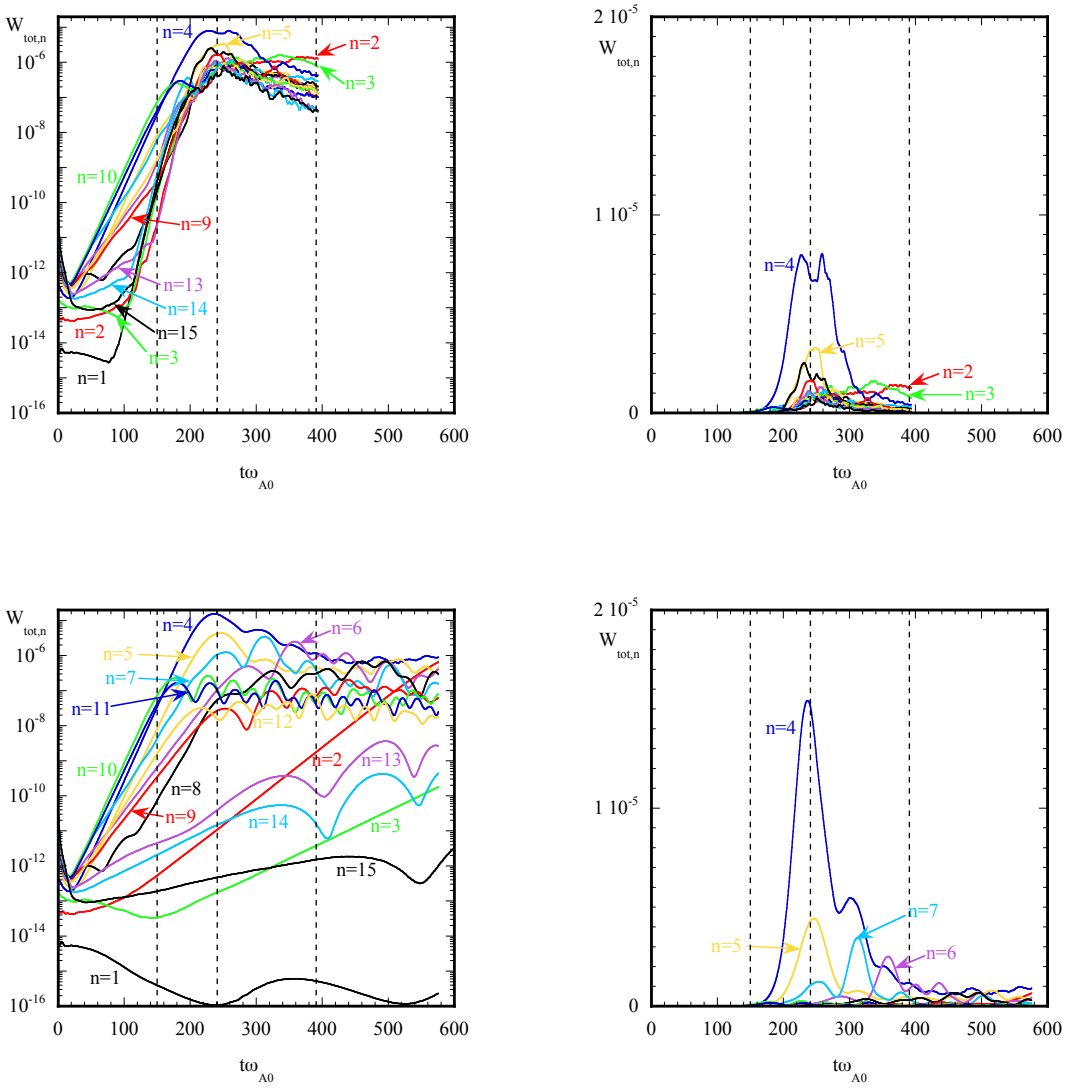

Figure 10. Multiple-n simulation (top frames) compared with the single-n simulations (bottom frames, see also Fig. 3): time evolution of the total (kinetic plus magnetic) MHD energy content for each toroidal mode number n considered $W_{\mathrm{tot},n}$ (left: logarithmic scale; right: linear scale). The vertical dashed lines correspond to the times of simulation $t\omega_{A0} = 150$, $t\omega_{A0} = 240$ and $t\omega_{A0} = 390$.

phenomenology of the $1 \leqslant n \leqslant 15$ multiple-n simulation here described in detail, just continuing longer the slow decaying phase.

Figure 11 shows the power spectra of the electrostatic potential $\phi(r, \omega)$ at the time $t\omega_{A0} = 150$, i.e., during the linear growth phase of the strongest growing modes (e.g., $n = 4$). By comparing Fig. 11 with the analogous figure for the single-n simulations, Fig. 5, it is evident how the power spectra of the subdominant modes are strongly modified: see, e.g., the $n \leqslant 3$ (in particular, the $n = 1$ mode, which, in the multiple-n simulation exhibits a frequency peak at a value close to zero, as the results of the

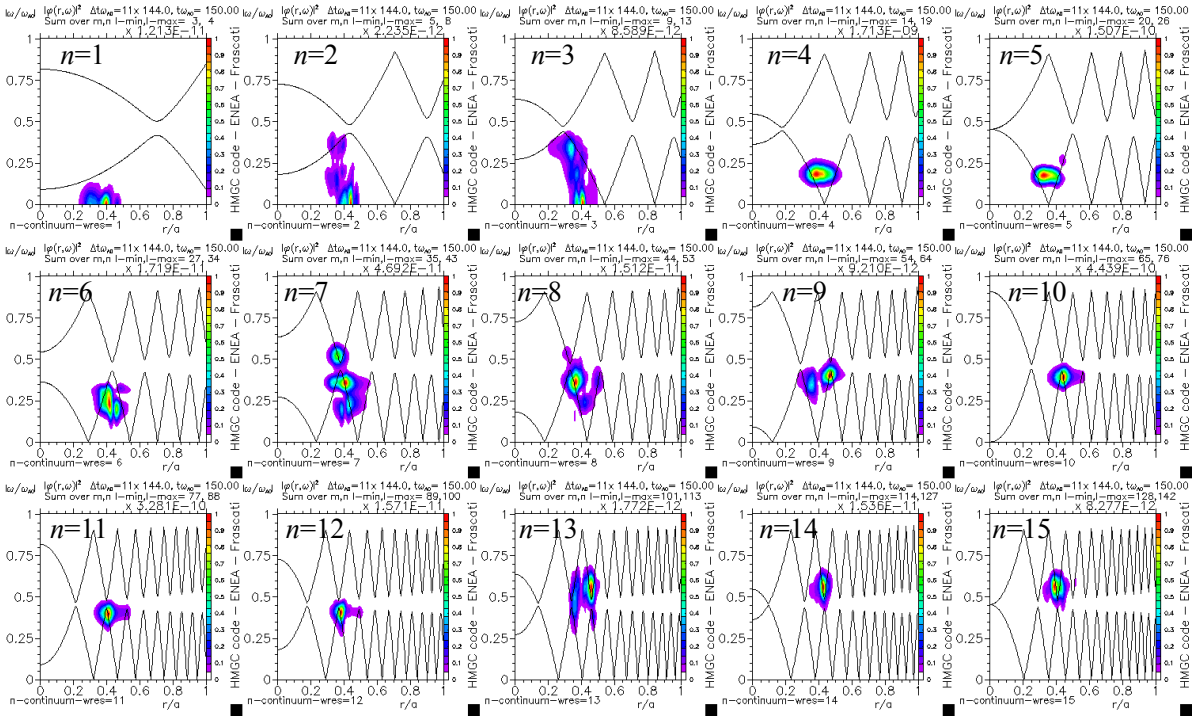

Figure 11. Power spectra of the electrostatic potential $\phi(r,\omega)$ for the multiple-n simulation (each frame refers to a specific toroidal mode number n), at $t\omega_{A0} = 150$ (see the first dashed vertical line in Fig. 10); solid lines refer to the (analytically computed) Alfvén continua.

beating between the dominant $n = 4, 5$ modes) and $n \geqslant 13$ modes, which, in the multiple-n simulation exhibit their frequency peaks at higher values than the ones in Fig. 5.

In Fig. 12 the radial profiles of the absolute value of the Fourier components of the electrostatic potential $|\phi_{m,n}|$ are reported, both for the single-n and multiple-n simulations, for few example toroidal mode numbers, namely $n = 1, 4, 5$. Comparing the radial profiles of the multiple-n simulation (Fig. 12, bottom row) with the corresponding ones of the single-n simulations (Fig. 12, top row), it can be appreciated how the nonlinear terms strongly modify the shape of the MHD fields of the $n = 1$, subdominant component, while the dominant Fourier components (e.g., $n = 4, 5$ in Fig. 12) remain almost unchanged in shape.

Note that the occurrence of almost simultaneous saturation of the whole Fourier spectrum is largely independent on the initial conditions of the simulations: in particular, reducing the amplitude A_n (see Eq. 8) of the subdominant modes by a factor up to 10^{-5} do not modify qualitatively the results.

The effect of considering simultaneously, and self-consistently, the evolution of multiple toroidal mode numbers n in a single simulation, including nonlinear coupling, is quite considerable in particular on the radial diffusion of the EP radial density profile, as shown in Fig. 13, where the multiple-n simulation is compared with the strongest

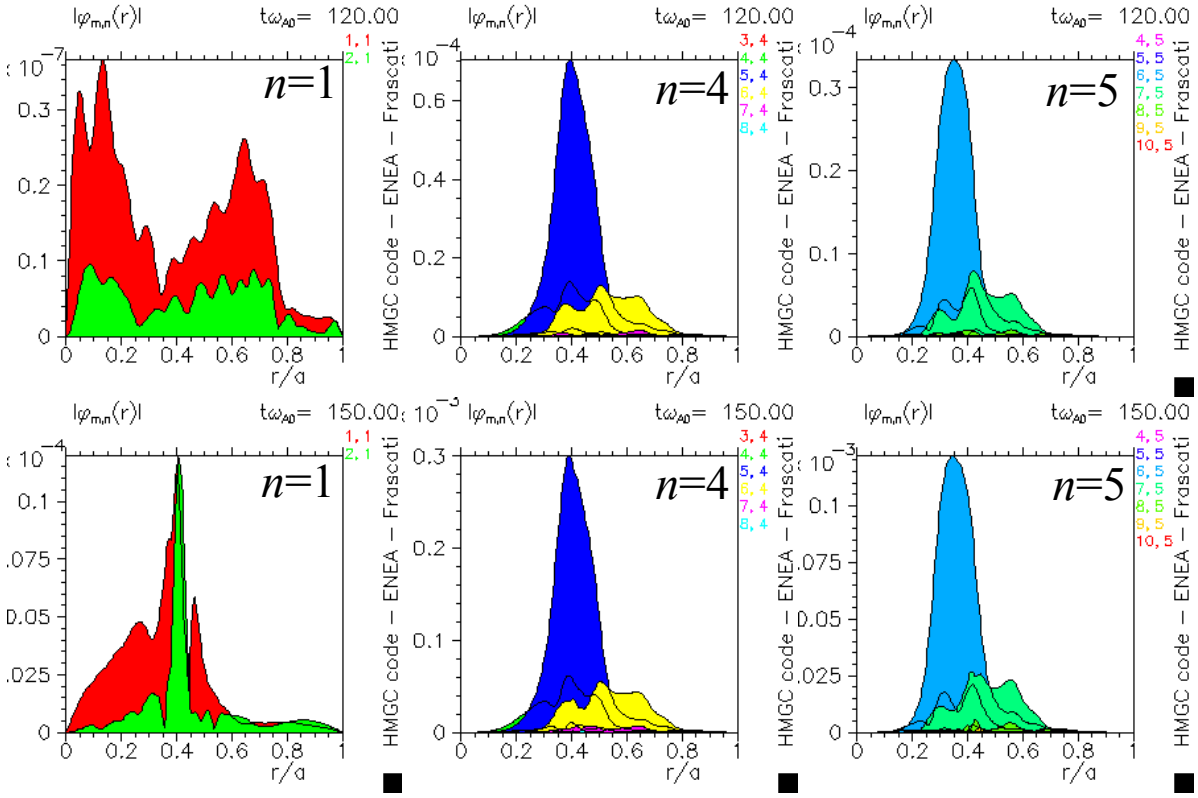

Figure 12. Radial profiles of the absolute value of the Fourier components of the electrostatic potential for the toroidal mode numbers $n = 1, 4, 5$ during the linear growth phase of the dominant modes: single-n simulations, $t\omega_{A0} = 120$ (top row), and multiple-n simulation, $t\omega_{A0} = 150$ (bottom row).

single-n one, i.e., $n = 4$, at the end of the multiple-n simulation ($t\omega_{A0} = 390$, see Fig. 10). The radial diffusion observed in the multiple-n simulation is considerably larger the one observed in the single-n, $n = 4$, case. Figure 13 shows the radial broadening of the EP distribution function at saturation, after integration over the whole velocity space. A more relevant variation is, in fact, observed if only the fraction of EPs which maximize the wave-particle power exchange is considered [8, 60, 64]. This is shown in Fig. 14, where $\hat{F}$ is plotted for initial and saturation phases. Here, $\hat{F}$ is the distribution function integrated over the portion of velocity space in which the wave-particle power exchange for the dominant Fourier component $n = 4$ is within 10% of its maximum. The reason of the enhanced EP radial diffusion as observed in the multiple-n simulation is suggested by Fig. 15, where the poloidal component of the fluctuating electric field E_θ for the multiple-n simulation and for the single-n, $n = 4$ one, are compared: a larger maximum absolute value in the plane (r, θ) (almost a factor of two, despite the $n = 4$ Fourier component of the single-n simulation is larger than the $n = 4$ Fourier component of the multiple-n one), a wider radial extension of the fluctuating electric field component considered, as well as a wider, in frequency, power spectrum are, indeed, observed.

To gain some insight on the relative importance between the different nonlinear terms entering the hybrid MHD-gyrokinetic model here considered, we have performed

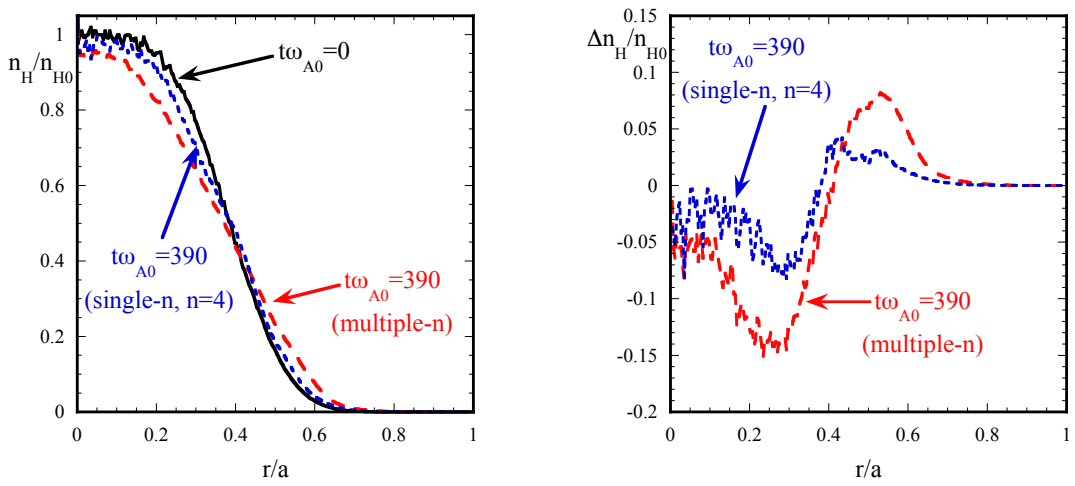

Figure 13. Comparison between multiple-n (blue, short dashed curve) and single-n, $n = 4$ (red, long dashed curve) simulations: left, EP radial density profile, right, $\Delta n_{\rm H}/n_{\rm H0} \equiv [n_{\rm H}(t = 390) - n_{\rm H}(t = 0)]/n_{\rm H0}$.

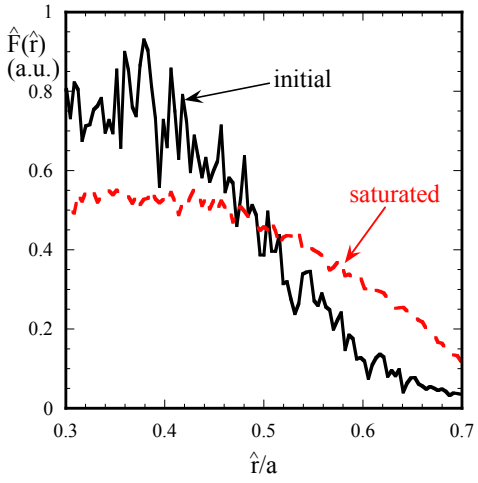

Figure 14. Initial (solid, black curve), and saturated (dashed, red curve) radial profile of the energetic particle distribution function $\hat{F}(\hat{r})$. Here, $\hat{F}$ is the distribution function integrated over the portion of velocity space in which the wave-particle power exchange for the dominant Fourier component $n = 4$ is within 10% of its maximum, and $\hat{r}$ is the radial coordinate the energetic particle gets when crossing the equatorial plane at its outmost R position.

a further multiple-n simulation in which, artificially, the nonlinear MHD terms are neglected. In this simulation, only $1 \leqslant n \leqslant 10$ have been considered. The results are shown in Fig. 16, where the time evolution of the total (kinetic plus magnetic) MHD

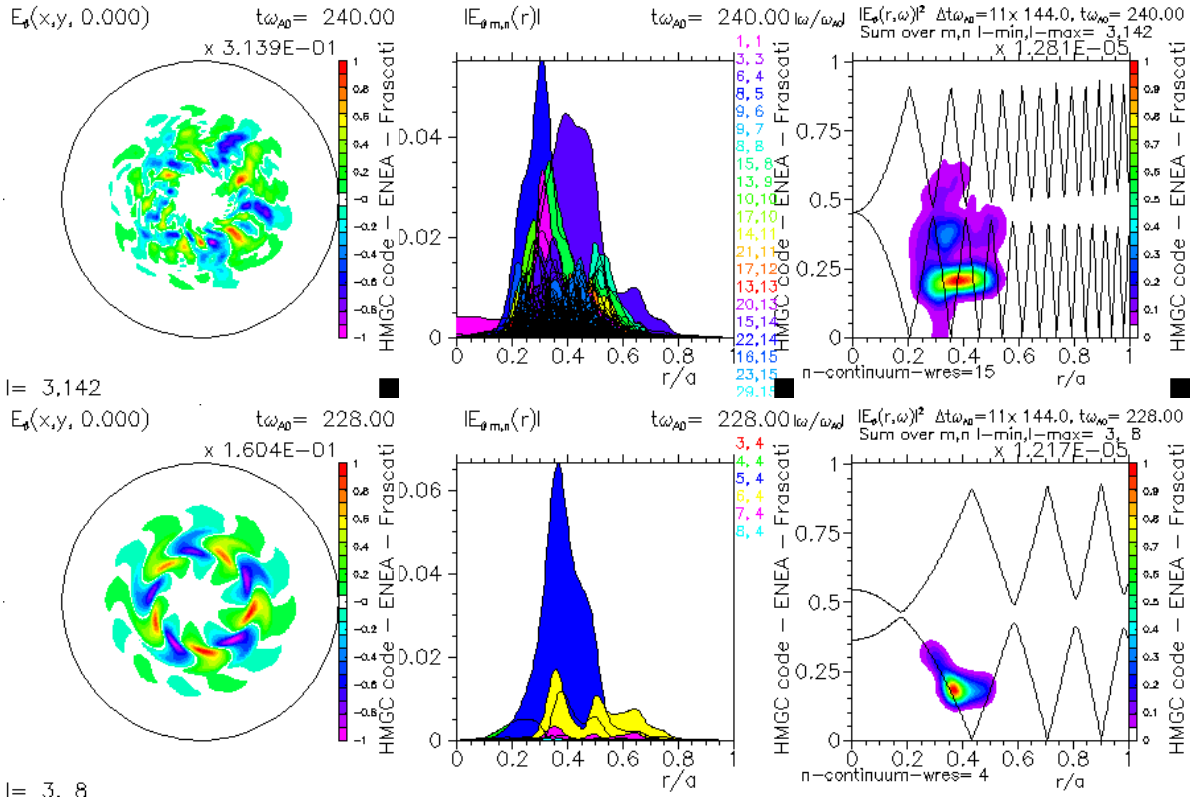

Figure 15. Poloidal component of the fluctuating electric field E_θ of the multiple-n simulation (top row, $t\omega_{A0} = 240$) compared with the single-n, $n = 4$ simulation (bottom row, $t\omega_{A0} = 228$) at the time corresponding to the maximum of the overshooting: $E_\theta(r,\theta)$ (left column); $|E_{\theta;m,n}(r)|$ (center column); power spectrum $|E_\theta(r,\omega)|^2$ (right column). Note that the Alfvén continuum for $n = 15$ is shown for the multiple-n simulation whereas the Alfvén continuum for $n = 4$ is shown for the single-n, $n = 4$ simulation.

energy content for the single-n simulations are compared, for each value of n, with the corresponding evolution in the multiple-n simulation with and without wave-wave coupling.

A first consideration to be drawn is that the wave-particle coupling, by itself, is able to drive nonlinearly unstable low-n modes (see the blue, long dashed curves in Fig. 16). When wave-wave coupling is introduced, the growth of the sub-dominant modes begins to grow earlier in time, without modifying the resulting growth-rate; a larger overshooting is also observed at saturation. The nonlinear effects are negligible on the fastest growing modes ($n = 4, 5, 10$); only the $n = 10$ mode exhibits a second nonlinear growth phase after the first roll over of saturation ($t\omega_{A0} \approx 250$).

The appearance of the wave-particle coupling of different toroidal mode numbers can be understand as follows, in the frame of a three-waves scheme. The EP drive enter the reduced-MHD equation, Eq. 2 through the $\nabla \cdot \mathbf{\Pi}_\mathrm{H}$ term, which is, on turn, proportional to the perturbed distribution function $\overline{F}_\mathrm{H}$ (see Eq. 3). The Vlasov equation, Eq. 7 can be rewritten, after introducing $\delta\overline{F}_\mathrm{H} \equiv \overline{F}_\mathrm{H} - \overline{F}_{\mathrm{H,eq}}$ (with $\overline{F}_{\mathrm{H,eq}}$ the equilibrium

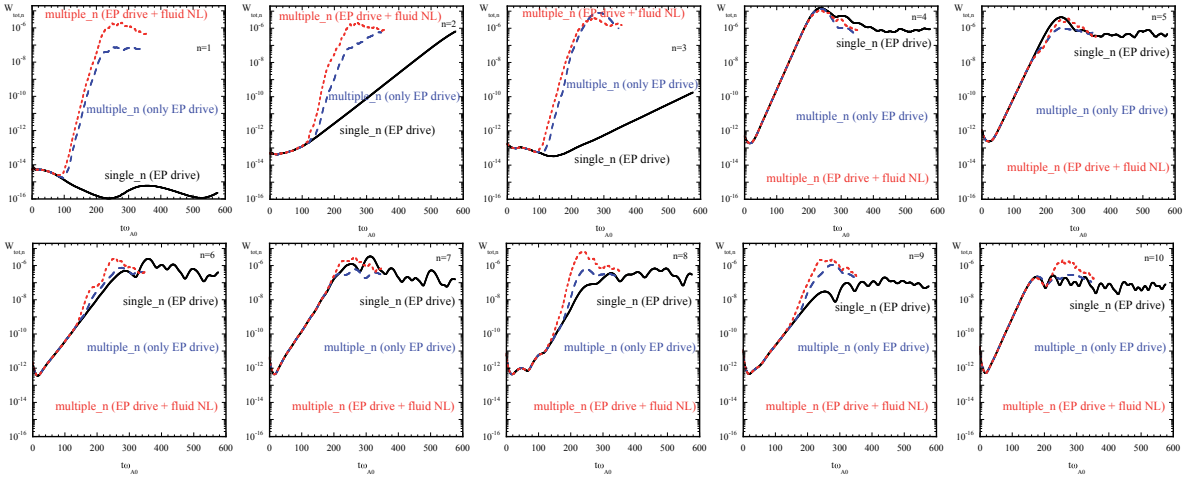

Figure 16. Time evolution of the total (kinetic plus magnetic) energy content $W_{\mathrm{tot},n}$, for each toroidal mode number n, for the single-n simulations (black, continuous curves), with the corresponding evolution of the multiple-n with only EP drive nonlinearities (blue, long dashed curves) and with the multiple-n simulation including both EP drive and fluid (MHD) nonlinearities (red, short dashed curves).

EP distribution function):

$$\left(\frac{\partial}{\partial t}+\frac{d\overline{Z}^i}{dt}\frac{\partial}{\partial \overline{Z}^i}\right)\delta\overline{F}_{\mathrm{H}} = -\left(\frac{d\overline{Z}^i}{dt}\right)_{\mathrm{pert}}\frac{\partial}{\partial \overline{Z}^i}\overline{F}_{\mathrm{H,eq}}\,, \tag{9}$$

where the subscript "pert" stands for perturbed quantities. After formally splitting the generalized velocities in the l.h.s. in equilibrium, "eq", and perturbed, "pert", contributions, the Vlasov equation written in term of $\delta\overline{F}_{\mathrm{H}}$, Eq. 9, becomes:

$$\begin{aligned}\left[\frac{\partial}{\partial t}+\left(\frac{d\overline{Z}^i}{dt}\right)_{\mathrm{eq}}\frac{\partial}{\partial \overline{Z}^i}\right]\delta\overline{F}_{\mathrm{H}} = & -\left(\frac{d\overline{Z}^i}{dt}\right)_{\mathrm{pert}}\frac{\partial}{\partial \overline{Z}^i}\overline{F}_{\mathrm{H,eq}} \\ & -\left(\frac{d\overline{Z}^i}{dt}\right)_{\mathrm{pert}}\frac{\partial}{\partial \overline{Z}^i}\delta\overline{F}_{\mathrm{H}}\,.\end{aligned} \tag{10}$$

After transforming in Fourier space along the toroidal direction, and considering that the equilibrium corresponds to $n=0$ Fourier toroidal component, the following expression is obtained for the n-th toroidal Fourier component of $\delta\overline{F}_{\mathrm{H}}$, $\delta\widehat{\overline{F}}_{\mathrm{H},n}$:

$$\begin{aligned}\left[\frac{\partial}{\partial t}+\left(\widehat{\frac{d\overline{Z}^i}{dt}}\right)_{0}\frac{\partial}{\partial \overline{Z}^i}\right]\delta\widehat{\overline{F}}_{\mathrm{H},n} = & -\left(\widehat{\frac{d\overline{Z}^i}{dt}}\right)_{n}\frac{\partial}{\partial \overline{Z}^i}\left(\widehat{\overline{F}}_{\mathrm{H};0}+\delta\widehat{\overline{F}}_{\mathrm{H};0}\right) \\ & -\Sigma_{\tilde{n}\neq 0}\left(\widehat{\frac{d\overline{Z}^i}{dt}}\right)_{n-\tilde{n}}\frac{\partial}{\partial \overline{Z}^i}\delta\widehat{\overline{F}}_{\mathrm{H};\tilde{n}}\end{aligned} \tag{11}$$

where the "hat" symbol indicates Fourier transformed quantities. The first term on r.h.s. (present in single-n simulations, as well) is the most important for the saturation

of the most unstable mode; it could also cause the nonlinear drive of subdominant modes by domino effect. The last, convolution term, gives rise to the three-waves NL coupling through the EP term. In Fig. 17 the time evolution of the drive for the $n = 1$, $n = 4$ and $n = 5$ modes is reported. It is apparent that the sudden transition from a quasi-

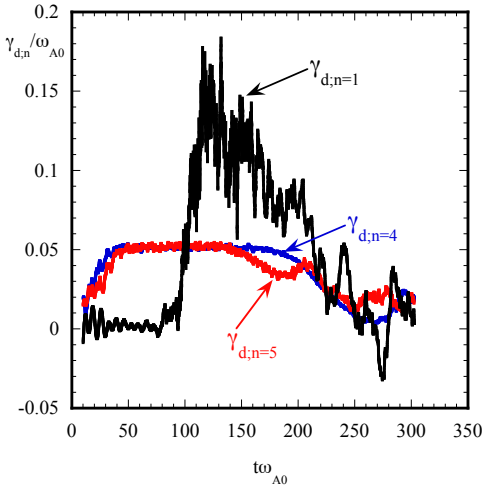

Figure 17. Time evolution of the drive $\gamma_{d;n}$ for the modes $n = 1$ (black curve), $n = 4$ (blue curve) and $n = 5$ (red curve).

marginally stable mode to a strongly driven mode for $n = 1$ (at $t\omega_{A0} \sim 100$) is mainly due to the contribution of $n = 4$ and $n = 5$ modes to the latter term. The domino effect does not play a relevant role, as it would require a significant modification of the $n = 0$ component of the distribution function ($\delta\overline{F}_{\mathrm{H};0}$) induced by the nonlinear interaction of energetic particles with the $n = 4$ and/or $n = 5$ modes. The fact that these two modes still exhibit, at $t\omega_{A0} \sim 100$, a constant drive shows that such modification has not yet occurred.

The effect of including wave-wave nonlinearities on the EP radial transport can be appreciated from Fig. 18. Wave-wave nonlinearities clearly add an important contribution to the radial broadening of the EP density profile, as it would be expected considering the larger overshooting of the saturated total energies on most of the toroidal components when considering also these terms (see Fig. 16).

4. Discussion and Conclusions

In this paper we have presented a systematic comparison between single-n and multiple-n self-consistent simulations of EP driven Alfvén modes in a low aspect ratio toroidal equilibrium using the hybrid MHD-gyrokinetic code HMGC. Toroidal mode numbers $1 \leqslant n \leqslant 15$ have been considered, keeping fixed all the physical

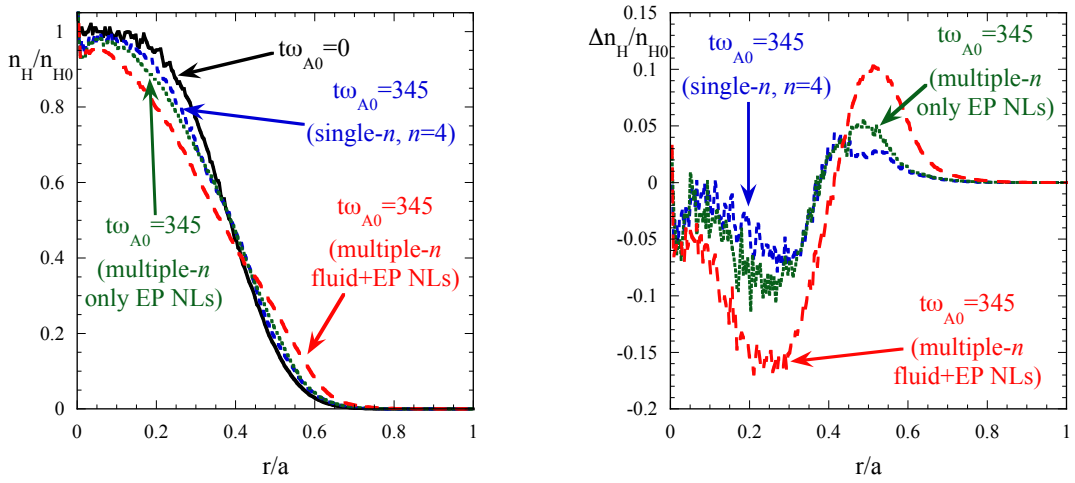

Figure 18. Effect of considering only the nonlinear terms coming from the EP or also the fluid (MHD) ones on the modification of the radial density profile of the EPs: left, EP radial density profile, right, $\Delta n_{\rm H}/n_{\rm H0} \equiv [n_{\rm H}(t=345) - n_{\rm H}(t=0)]/n_{\rm H0}$. Black, solid curve is at $t\omega_{A0} = 0$; blue, short dashed curve is single-n ($n = 4$) at $t\omega_{A0} = 345$ (here reported only for reference); green, dotted curve is multiple-n at $t\omega_{A0} = 345$ considering only EP nonlinearities; red, long dashed curve is multiple-n at $t\omega_{A0} = 345$ considering both EP and fluid (MHD) nonlinearities.

and numerical parameters of the simulations, considering both wave-wave and wave-particle nonlinearities. Single-n simulations exhibit several stable $n = 1$ modes, whereas moderately unstable modes are observed for $n = 2, 3$ and $n = 13, 14, 15$, and strongly unstable ones for $4 \leqslant n \leqslant 12$. A variety of different modes are indeed identified: GAEs, TAEs, KTAEs and EPMs. Growth-rates are larger for $4 \leqslant n \leqslant 12$, then decreasing with increasing toroidal mode number n. On the other side, maximum saturation amplitude is larger for $n = 4$ and decreases evidently as toroidal mode number increases. Regarding the nonlinear saturation, induced by wave-particle nonlinearities, all the single-n simulations which reach nonlinear regime exhibit both up and down frequency chirping, and the analysis of the power exchange between EPs and wave reveals that, depending on n numbers, either trapped particles or circulating particles are responsible for driving the modes. Considering the effects of such modes on the EP radial density profile, although some of the modes observed are driven quite strongly (for $n = 4$, e.g., the ratio of the growth-rate γ to the mode frequency ω_0 is $\gamma/\omega_0 \gtrsim 0.25$), the broadening that occurs after saturation is quite modest.

When comparing the single-n simulations with the multiple-n ones, in which both wave-wave and wave-particle nonlinearities are retained, several interesting elements deserve to be pointed out. First, it is observed that sub-dominant modes ($n \leqslant 3$ and $n \geqslant 13$), are already driven strongly unstable during the linear growth phase of the dominant modes ($4 \leqslant n \leqslant 12$). The radial shape of the MHD fields of these sub-

dominant modes are strongly modified by nonlinear coupling, having no relation with the eigenfunctions shown in the linear phase of the single-n simulations (see, e.g., Fig. 12 and also compare Fig. 5 and Fig. 11 which show the power spectra), demonstrating the importance of self-consistent simulations where the interaction between different toroidal modes is fully retained. Saturation of all the modes considered in the multiple-n simulations occurs almost simultaneously: a similar behaviour has been shown in Refs. [36, 65], where the hybrid MHD-gyrokinetic code MEGA was used, although a detailed comparison with single-n simulations is missing. No evidence of the so-called "domino" effect is observed in our multiple-n simulations, contrary to what observed in Ref. [40], where, however, it should be noted that mode structures, as obtained by linear codes, were kept fixed in time during their simulations, and only their amplitudes and frequencies were allowed to vary. Our multiple-n simulations show a clear enhancement of EP density transport w.r.t. the single-n ones (see, e.g., Fig. 18), and this can be traced back to an enhancement of the maximum amplitude of the overall electromagnetic field reached at saturation (despite the $n = 4$ Fourier component of the single-n simulation is larger than the $n = 4$ Fourier component of the multiple-n one), together with both its wider radial extension and wider, in frequency, power spectrum. As already stated above, the model equilibrium chosen in this paper is characterized by a quite large linear growth-rate of the dominant modes ($\gamma/\omega_0 \gtrsim 0.25$); indeed, whether in practical applications the system will reach or not a condition near marginal stability, where dissipation balances drive, depends on how strongly the system itself is driven. The main issue is how much and in which way the system will fluctuate about some (spatiotemporal) "average", which may or may not be marginally stable. This point is discussed at length in a recent review paper [8]. Moreover, the evolution of $n = 0$ Fourier component has not been considered here: this means that the eventual formation of so-called zonal structures by shear Alfvén waves (see, e.g., Refs. [8, 42]), which are known to be able to regulate the turbulence induced transport, have not been considered in the present simulations, and will require further future investigations.

Acknowledgments

This work has been carried out within the framework of the EUROfusion Consortium and has received funding from the Euratom research and training programme 2014-2018 under grant agreement No 633053. The views and opinions expressed herein do not necessarily reflect those of the European Commission. Part of the computing resources and the related technical support used for this work have been provided by the EUROfusion High Performance Computer (Marconi-Fusion [41]) hosted by CINECA Bologna (Italy) and part by the CRESCO/ENEAGRID High Performance Computing infrastructure and its staff [66].

References

[1] Aymar R., Chuyanov V., Huguet M., Parker R., Shimamura Y., and the ITER Joint Central Team and Home Teams 1997 in *Proceedings of the 16th International Conference on Fusion Energy* 1996, Vol. 1 (International Atomic Energy Agency, Vienna), p. 3

[2] ITER Physics Basis Editors, et al. 1999 *Nucl. Fusion* **39** 2137

[3] ITER Physics Basis Expert Groups on Confinement and Transport and Confinement Modelling and Database, ITER Physics Basis Editors 1999 *Nucl. Fusion* **39** 2175

[4] Heidbrink W.W. and Sadler G.J. 1994 *Nucl. Fusion* **34** 535

[5] Wong K. 1999 *Plasma Phys. Control. Fusion* **42** R1

[6] Breizman B. and Sharapov S. 2011 *Plasma Phys. Control. Fusion* **53** 054001

[7] Gorelenkov N.N., Pinches S.D. and Toi K. 2014 *Nucl. Fusion* **54** 125001

[8] Chen L. and Zonca F. 2016 *Rev. Mod. Phys.* **88** 015008, DOI: 10.1103/RevModPhys.88.015008

[9] Lauber Ph. 2013 *Phys. Rep.* **533** 33

[10] Spong D.A., Carreras B.A. and Hedrick C.L. 1992 *Phys. Fluids B*, **4** 3316

[11] Cheng C.Z. 1992 *Phys. Rep.*, **211** 1

[12] Mikhailovskii A.B., Huysmans G.T.A., Sharapov S.E. and Kerner W.O. 1997 *Plasma Phys. Rep.* **23** 844

[13] Pinches S.D. et al. 1998 *Comput. Phys. Commun.*, **111** 131

[14] Gorelenkov N.N., Cheng C.Z. and Fu G.Y. 1999 *Phys. Plasmas*, **6** 2802

[15] Borba D. et al. 2002 *Nucl. Fusion*, **42** 1029-1038

[16] Liu Y.Q., Chu M.S., Chapman I.T. and Hender T.C. 2008 *Phys. Plasmas*, **15** 112503

[17] Zheng L.J., Kotschenreuther M.T. and Van Dam J.W. 2010 *J. Comput. Phys.*, **229** 3605

[18] Park W. et al. 1992 *Phys. Fluids B*, **4** 2033

[19] Briguglio S., Vlad G., Zonca F. and Kar C 1995 *Physics of Plasmas*, **2** 3711-3723

[20] Todo Y., Sato T., Watanabe K., Watanabe T.H. and Horiuchi R. 1995 *Phys. Plasmas*, **2** 2711

[21] Briguglio S., Zonca F. and Vlad G. 1998 *Physics of Plasmas*, **5** 3287-3301

[22] Todo Y. and Sato T. 1998 *Phys. Plasmas*, **5** 1321

[23] Park W., Belova E.V., Fu G.Y., Tang X.Z., Strauss H.R. and Sugiyama L.E. 1999 *Phys. Plasmas* **6** 1796

[24] Todo Y., Shinohara K., Takechi M. and Ishikawa M. 2005 *Phys. Plasmas*, **12** 012503

[25] Todo Y. 2006 *Phys. Plasmas*, **13** 082503

[26] Wang X., Briguglio S., Chen L., Di Troia C., Fogaccia G., Vlad G. and Zonca F. 2011 *Phys. Plasmas*, **18** 052504

[27] Cole M., Mishchenko A., Könies A., Kleiber R., and Borchardt M 2014 *Phys. Plasmas* **21** 072123

[28] Mishchenko A., Könies A. and Hatzky R. 2009 *Phys. Plasmas*, **16** 082105

[29] Deng W., Lin Z., Holod I., Wang X., Xiao Y. and Zhang W. 2010 *Phys. Plasmas*, **17** 112504

[30] Cole M.D.J., Mishchenko A., Könies A., Hatzky R. and Kleiber R. 2015 *Plasma Phys. Control. Fusion*, **57** 054013

[31] Vlad G, Kar C, Zonca F and Romanelli F 1995 *Physics of Plasmas*, **2** 418-441.

[32] Brizard A.J. and Hahm T.S. 2007 *Rev. Mod. Phys.*, **79** 421-468

[33] Todo Y., Berk H.L. and Breizman B.N. 2010 *Nucl. Fusion* **50** 084016

[34] Todo Y., Berk H.L. and Breizman B.N. 2012 *Nucl. Fusion* **52** 094018

[35] Todo Y., Berk H.L. and Breizman B.N. 2012 *Nucl. Fusion* **52** 033003

[36] Todo Y. and Bierwage A. 2014 *Plasma and Fusion Research* **9** 3403068

[37] Todo Y., Van Zeeland M.A., Bierwage A., Heidbrink W.W. and Austin M.E. 2015 *Nucl. Fusion* **55** 073020

[38] Todo Y., Van Zeeland M.A. and Heidbrink W.W. 2016 *Nucl. Fusion* **56** 112008

[39] Todo Y. 2016 *New J. Phys.* **18** 115005

[40] Schneller M., Lauber Ph. and Briguglio S. 2016 *Plasma Phys. Contr. Fusion* **58** 014019

[41] Iannone F. et al 2017 *Fusion Engineering and Design* in press

[42] Diamond P.H., Itoh S.-I., Itoh K. and Hahm T.S. 2005 Plasma Phys. Controlled Fusion **47** R35
[43] Cheng C.Z., Chen Liu and Chance M.S. 1985 *Ann. Phys.* (N.Y.) **161** 21
[44] Izzo R., Monticello D.A., Park W., Manickam J., Strauss H.R., Grimm R. and McGuire K. 1983 *Phys. Fluids* **26** 2240
[45] Vlad G., Zonca F. and Briguglio S. 1999 *Rivista del Nuovo Cimento* **22** 1–97
[46] Zonca F. and Liu Chen 1993 *Phys. Fluids* **B 5** 3668
[47] Fu G.Y. and Cheng C.Z. 1992 *Phys. Fluids* **B 4** 3722
[48] Berk H.L., Breizman B.N. and Ye H. 1992 *Phys. Lett. A* **162** 475
[49] Tsai S.T. and Chen L. 1993 *Phys. Fluids* **B 5** 3284
[50] Zonca F. and Chen L. 1996 *Phys. Plasmas* **3** 323
[51] Mahajan S.M. 1995 *Phys. Scr.* **T60** 160
[52] Mett R.R. and Mahajan S.M. 1992 *Phys. Fluids B* **4** 2385
[53] Chen Liu 1994 *Phys. Plasmas* **1** 1519
[54] Zonca F., Chen L., Briguglio S., Fogaccia G., Vlad G. and Wang X. 2015 *New J. Phys.* **17** 013052
[55] Vlad G., Fusco V., Briguglio S., Fogaccia G., Zonca F. and Wang X. 2016 *New J. Phys.* **18** 105004
[56] Berk H.L., Breizman B.N. and Petiashvili N.V. 1997 *Phys. Lett. A* **234** 213
[57] Breizman B.N., Berk H.L., Pekker M., Porcelli F., Stupakov G.V. and Wong K.L. 1997 *Phys. Plasmas* **4** 1559
[58] Berk H.L., Breizman B.N., Candy J., Pekker M. and Petiashvili N.V. 1999 *Phys. Plasmas* **6** 3102
[59] White R.B. 2012 *Commun. Nonlinear Sci. Numer. Simulat.* **17** 2200–2214
[60] Briguglio S., Wang X., Zonca F., Vlad G., Fogaccia G., Di Troia C. and Fusco V. 2014 *Phys. Plasmas*, **21** 112301
[61] Berk H.L. and Breizman B.N. 1990 *Phys. Fluids B* **2** 2226
[62] Berk H.L. and Breizman B.N. 1990 *Phys. Fluids B* **2** 2235
[63] Berk H.L. and Breizman B.N. 1990 *Phys. Fluids B* **2** 2246
[64] Briguglio S., Schneller M., Wang X., Di Troia C., Hayward-Schneider T., Fusco V., Vlad G. and Fogaccia G. 2017 *Nucl. Fusion*, **57** 072001
[65] Todo Y. 2017 Paper presented at the 2017 IAEA Technical Meeting on "Energetic Particles in Magnetic Confinement Systems", 5-8 September 2017,Princeton, NJ, USA
[66] Ponti G. et al. 2014 *Proceedings of the 2014 International Conference on High Performance Computing and Simulation, HPCS 2014*, art. no. 6903807, 1030-1033.